ACS APPLIED NANO MATERIALS

www.acsanm.org

Article

Biocompatible Polyelectrolyte Multilayers with Copper Oxide and Zinc Oxide Nanoparticles for Inhibiting Bacterial Growth

Nives Matijaković Mlinarić,* Stefanie Altenried, Atiđa Selmani, Juraj Nikolić, Aleksander Učakar, Anamarija Zore, Anže Abram, Sandro Lehner, Andrijana Sever Škapin, Monika Kušter, Eva Roblegg, Davor Kovačević, Qun Ren, and Klemen Bohinc*

Cite This: https://doi.org/10.1021/acsanm.4c00981

Read Online

ACCESS | Metrics & More | Article Recommendations | Supporting Information

ABSTRACT: The prevalence of bacterial infections presents a significant challenge in the medical field, demanding effective strategies to impede bacterial adhesion and growth on various surfaces. The conducted study investigates the efficacy of polyelectrolyte multilayers—comprising poly(allylamine hydrochloride) (PAH) and alginate (ALG)—embedded with zinc oxide (ZnO) and copper oxide (CuO) nanoparticles (NPs) to inhibit bacterial adhesion on stainless-steel surfaces. Surface characterization involved zeta potential, contact angle, and roughness assessments. The effect of NP composition, size, and morphology in conjunction with polycation or polyanion terminating multilayers was evaluated against planktonic and surface-adhered *Escherichia coli* (*E. coli*) cells. Surfaces with the positively charged PAH-terminating multilayer displayed higher water contact angles (≈ 63°) than the negatively charged ALG-terminating multilayers (≈ 45°). Multilayers containing ZnO NPs showed a significant inhibition of planktonic *E. coli* growth, >99%. Moreover, complete growth inhibition of surface-adhered *E. coli* was achieved for multilayers containing both ZnO and CuO. Due to their larger specific surface area, rod-like ZnO NPs displayed higher antibacterial activity. The samples with ALG as the terminating layer showed more substantial antibacterial properties than samples with PAH as the terminating layer. Biocompatibility tests on immortalized human keratinocyte cells revealed good compatibility with multilayers incorporating NPs. In summary, this study underscores the potential of ZnO and CuO NPs within PAH/ALG multilayers for antibacterial applications without compromising their cytocompatibility.

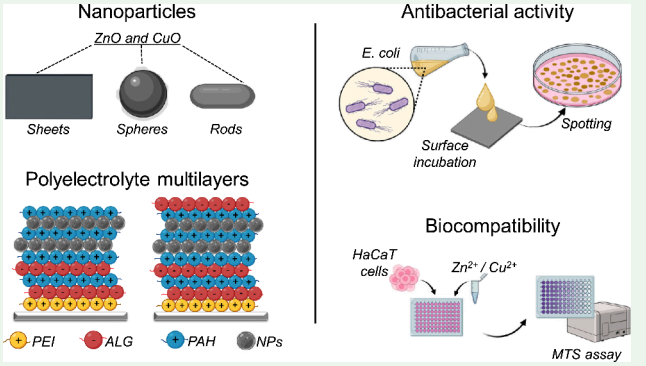

KEYWORDS: *polyelectrolyte multilayers, alginate, poly(allylamine hydrochloride), CuO, ZnO, nanoparticles, Escherichia coli*

1. INTRODUCTION

Bacterial infections, originating primarily from the human bacterial flora, constitute some of the most critical medical challenges. While bacterial microbiota play a pivotal role in human physiology, they concurrently harbor pathogenic strains capable of inducing a spectrum of infections.[1] *Escherichia coli* (*E. coli*), a commensal strain in the human gastrointestinal tract, typically coexists with its host in a mutually beneficial way. Nonetheless, specific *E. coli* strains can potentially cause extra-intestinal and urinary infections, sepsis, meningitis, and enteric ailments like dysentery and diarrhea.[2]

Bacterial adherence and proliferation across diverse surfaces such as glass, various polymers, aluminum, and stainless-steel have been observed.[3,4] In hospital settings, numerous surfaces, including prostheses, surgical instruments, implants, urinary and cardiovascular catheters, can serve as breeding grounds for bacterial colonization.[5−7] Consequently, preventing bacterial adhesion and growth on such surfaces remains imperative.

Nanomaterials emerged as an elegant strategy to mitigate bacterial infections. Due to their superior intrinsic properties, such as small size, high surface-to-volume ratio, various morphologies, and optical properties, nanomaterials are recognized as the next generation of antibacterial agents.[8] Nanomaterials have found applications ranging from drug treatment[9] to food additives.[10] Notably, metal and metal oxide nanoparticles (NPs), such as silver (Ag), copper oxide (CuO), titanium dioxide (TiO_2), magnesium oxide (MgO), and zinc oxide (ZnO), exhibit favorable traits for antibacterial applications due to their durability, reduced toxicity to human cells, and robust stability.[11,12] Nanoparticle (NP) properties depend on their size, shape, crystallinity, surface structure, and surface charge. Higher antibacterial activity and

Received: February 17, 2024
Revised: April 26, 2024
Accepted: April 30, 2024

toxicity are obtained with smaller NP sizes.[13,14] Smaller NPs, compared to larger ones, have bigger surface areas, providing better contact with cells.[12] Furthermore, NP characteristics, including morphology (e.g., spheres, rods, needles, flowers, plates), surface chemistry, coatings with molecules, and stability, can modify their activity.[15]

ZnO[15−19] and CuO NPs[20,21] show good antibacterial activity against Gram-positive and Gram-negative bacteria. However, a comparative analysis of antibacterial activity considering various NP morphologies of ZnO and CuO[22,23] remains incomplete. ZnO and CuO NPs can be used for antibacterial applications, but their biocompatibility has to be determined. In healthcare, where contact with the human body occurs, biocompatibility with human tissue is crucial. The current findings highlight the need to address NP biosafety and modify NP surface reactivity to decrease adverse effects and enhance biocompatibility.[24] ZnO NPs and Zn^{2+} ions have exhibited potential for surface applications without causing skin irritation.[15] However, the literature indicates a cytotoxic effect of CuO NPs and Cu^{2+} ions, particularly pronounced in the NP form compared to dissolved ions.[25] Previous studies on orthotic textile materials treated with CuO NPs caused antibacterial effects against Gram-positive bacteria but also, due to loosely bound NPs, induced cytotoxic effects on human cells.[26] To limit the direct contact of NPs with human tissue, organic molecules, which show good biocompatibility, can lower the NP cytotoxic effect. The use of PAH multilayers for coating various textile materials resulted in ZnO NP immobilization with high antibacterial activity against Gram-positive bacteria and good biocompatibility with skin cells (keratinocytes).[27] Alginate (ALG) with gelatin and cellulose showed excellent biocompatibility with fibroblast cells and promising use for biomedical devices and artificial tissues.[28] Also, poly(allylamine hydrochloride) (PAH) and poly(ethylene glycol diacrylate) showed good biocompatibility with pig skin and exhibited antibacterial activity against Gram-positive bacteria and potential use for skin grafting.[29] In addition to good biocompatibility, the utilization of organic molecules for the production of coatings on surfaces holds the potential to deter bacterial adhesion, leveraging the repulsive force established between negatively charged bacterial cells and similarly charged coatings.[30,31] Multilayers have been used for various applications from cell prolifferation,[32] biomedical applications,[33,34] polymeric templates for NP synthesis[35,36] to antibacterial[37,38] applications alongside metal NPs.[39,40] While PAH/ALG multilayers have demonstrated compatibility with osteoblast cells,[41] their specific antibacterial effects and biocompatibility with and without NPs have not been investigated so far.

To bridge the aforementioned research gap, the study aimed to determine the difference in the antibacterial activity of ZnO and CuO with similar sizes and shapes in a way that the difference between them can be observed only due to different chemical compositions. Moreover, the antibacterial effect between NPs with different morphologies (sheets, rods and spheres) was determined. *E. coli* was used as a model bacterial pathogen. Furthermore, for the first time, PAH/ALG multilayers were employed to entrap CuO and ZnO NPs to limit cytotoxicity against human cells and to determine the coating's antibacterial activity. As well the more optimal terminating layer (PAH or ALG) for antibacterial and biocompatible applications was determined. For this purpose, stainless-steel surfaces were coated with polyelectrolyte multilayers (PAH/ALG) containing ZnO and CuO NPs. The formation of these polyelectrolyte multilayers was confirmed using ellipsometry and atomic force microscopy (AFM). Moreover, the surface's physicochemical characteristics were assessed by measuring the surface roughness, zeta potential, and water contact angle. The ions released from the coated surface were assessed using inductively coupled plasma optical emission spectrometry (ICP-OES). The coated surfaces were contaminated with the pathogen Gram-negative *E. coli* to test the antibacterial properties. Finally, for possible biomedical applications, surface biocompatibility was assessed toward immortalized human keratinocyte (HaCaT) cells.

2. EXPERIMENTAL SECTION

2.1. Synthesis of CuO and ZnO Nanoparticles. CuO and ZnO NPs were synthesized utilizing analytical grade reagents: $CuSO_4 \bullet 5H_2O$, $Zn(CH_3CO_2)_2 \bullet 2H_2O$, and NaOH purchased from Sigma-Aldrich. Reaction solutions were prepared by dissolving each salt in deionized water (conductivity < 0.055 $\mu S\ cm^{-1}$). The synthesis procedures (Table 1) for CuO involved adding 0.5 mL of NaOH (at concentrations of 1.0, 2.0, and 5.0 mol L^{-1}) to 2 mL of $CuSO_4$ solution ($c(CuSO_4)$ = 0.1 mol L^{-1}). The suspension was heated to 60 °C and magnetically stirred (300 rpm) until the color changed from blue to black. ZnO NPs were synthesized via a modified method (Table 1) from the literature.[42] A solution of $Zn(CH_3CO_2)_2$ (c = 0.1 mol L^{-1}) was prepared in a 5:1 water−ethanol mixture. ZnO NPs were obtained by adding 50 mL of NaOH to 150 mL of the $Zn(CH_3CO_2)_2$ solution. The first suspension with 1.0 mol L^{-1} NaOH was heated to 70 °C and magnetically stirred (300 rpm) for 15 min. The other two suspensions with 5.0 mol L^{-1} NaOH were heated to 85 °C for one and 2 h under magnetic stirring (300 rpm). The resulting NPs were separated via centrifugation (6000 rpm) and washed with deionized water through multiple cycles. The collected samples were dried at 100 °C for 5 h. The dried samples were annealed at 400 °C for 2 h using a Nabertherm furnace (Bremen, Germany) to obtain highly crystalline NPs. Subsequently, the annealed samples were dispersed in distilled water with ultrasound. To stabilize the NPs, 0.133 mL of sodium poly(4-styrenesulfonate) (PSS) (w = 0.5%, Sigma-Aldrich) was added to 10 mL of NP suspension.

Table 1. Experimental Parameters Used for the Preparation of CuO and ZnO Nanoparticles with Different Morphology

NPs type	c(NaOH) [mol L^{-1}]	θ [°C]	t [min]
CuO sheets[26]	1	60	15
CuO rods	5	70	15
CuO spheres	2	70	15
ZnO sheets	5	85	60
ZnO rods[27]	5	85	120
ZnO spheres	1	70	15

2.2. Nanoparticle Characterization. The morphology of the obtained NPs was examined using a Schottky field emission scanning electron microscope (SEM) Jeol JSM-7600F (Jeol Ltd., Tokyo, Japan). NP sizes were determined from SEM images using ImageJ software. Electrokinetic measurements in water were conducted utilizing a Zetasizer Ultra instrument (Malvern Panalytical, Malvern, United Kingdom) in a DTS 1070 Folded capillary cell at 25 °C. Zeta potential was derived from five measurements using Smoluchowski's approximations to convert electrophoretic mobility into zeta potential. The mean particle size in water at 25 °C was determined by dynamic light scattering (DLS) using the Zetasizer Ultra (Malvern Panalytical, Malvern, United Kingdom). Measurements were performed with 1.0 mL of sample (5 measurements per sample) in a disposable DTS0012 plastic cell. The initial mass concentration of NPs was 30 mg mL^{-1}. Hydrodynamic diameters were obtained from the Einstein-Stokes equation with the approximation that all NPs have spherical

https://doi.org/10.1021/acsanm.4c00981
ACS Appl. Nano Mater. XXXX, XXX, XXX−XXX

morphology. X-ray diffraction (XRD) analysis on polycrystalline samples confirmed the composition of ZnO and CuO NPs. Analysis was performed on a Malvern Panalytical Empyrean X-ray diffractometer (Almelo, Netherlands) with a Cu-target tube and a step size of 0.0131° and 1 s per step in the 2θ range of 20° − 80° in Bragg−Brentano geometry. PANalytical High Score Plus software was used to analyze the diffraction patterns. Fourier-transform infrared (FTIR) spectroscopy in the (340−4000) cm^{-1} range was employed to analyze CuO and ZnO NPs using the PerkinElmer FT-IR C89391 instrument (PerkinElmer, Massachusetts, USA). The specific surface areas of the samples were determined by the nitrogen adsorption method using ASAP 2020 Sorber (Micromeritics, USA) at −196 °C (77 K). The Brunauer−Emmett−Teller theory was applied to calculate specific surface areas after the samples were outgassed in a vacuum for 15 h at 120 °C.

2.3. Fabrication of the Multilayers. Multilayer coating was prepared with poly(ethyleneimine) (PEI, linear, average Mn 10,000, PDI ≤ 1.5), poly(allylamine hydrochloride) (PAH, average Mw ∼ 17,500), and alginate (ALG, Alginic acid sodium salt, powder, CAS Number: 9005−38−3), all purchased from Sigma-Aldrich. The PAH/ALG multilayer was fabricated using a modified LbL (Layer-by-Layer) method as previously described.[41] Stainless-steel plates (AISI 304 BA, obtained from Mihoković d.o.o., Zagreb, Croatia in dimensions: 10 mm × 10 mm × 0.8 mm) were cleaned in a 5 mol L^{-1} NaOH alkaline solution for 30 min and rinsed with water. The plates were then immersed in a PEI solution (5 g L^{-1}, pH = 10) for 30 min. Subsequently, the modified plates were subjected to multilayer deposition of $(ALG/PAH)_n$, where n represents the number of bilayers, through alternate immersion in ALG (3.0 g L^{-1}, pH 7.5) and PAH (3.0 g L^{-1}, pH 7.5) solutions for 15 min (Scheme 1). In this study, n = 2 was applied before adding 100 μL of NP suspension (115 μg mL^{-1}) between the last three PAH layers. The surface underwent coating with two layers of NP suspension. The coating process was finished with a final layer of PAH or ALG to assess the influence of positive or negative layers on antibacterial activity and cytocompatibility. After each layer deposition, the surface was rinsed with deionized water and dried with air.

Scheme 1. Multilayer Coating Prepared on the Stainless-Steel Surface (Light Gray Line) with Two Terminating Types of Layers, ALG (Red Spheres) and PAH (Blue Spheres)[a]

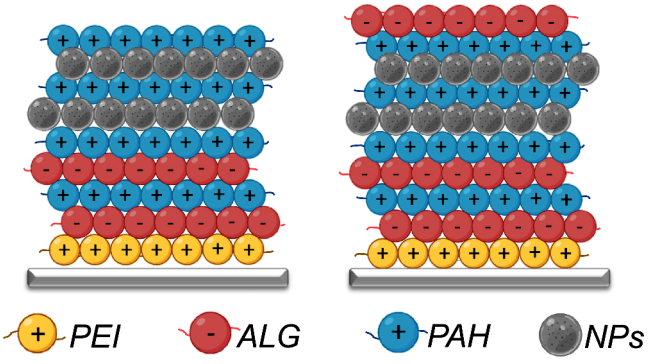

[a]The coating procedure was started with the initial layer of PEI (yellow spheres) followed by alternating PAH/ALG. ZnO and CuO nanoparticles (gray spheres) were applied between the last three PAH layers. PEI - poly(ethyleneimine), PAH − poly(allylamine hydrochloride), ALG - alginate.

2.4. Characterization of the Multilayers. The FTIR spectra of the stainless-steel plates coated with PAH/ALG multilayers embedded with ZnO and CuO NPs were measured on a Nicolet iS50 FTIR Spectrometer equipped with an ATR module. Each FTIR spectra was obtained as an average of 64 scans with a resolution of 4 cm^{-1}. Spectra of films containing different morphologies of CuO and ZnO nanoparticles were measured from (300−1800) cm^{-1}. As a background, a stainless-steel substrate was used with correction for H_2O and CO_2. On the other hand, PAH and ALG (in powder form) spectra were obtained with air used as a background. XRD analysis of the stainless-steel plates coated with PAH/ALG multilayers embedded with ZnO and CuO NPs was performed on a Malvern Panalytical Empyrean X-ray diffractometer (Almelo, Netherlands) with a Cu-target tube and a step size of 0.0131° and 1 s per step in the 2θ range of 15° − 80° in Bragg−Brentano geometry. The thickness of the multilayers was determined via ellipsometry measurements using the Ellipsometer L116B-USB (Gaertner Scientific Corporation, Skokie, USA). Experiments were conducted at room temperature and 30 to 50% relative humidity, employing a monochromatic laser beam (λ = 632.8 nm) incident on the sample surface at a 70° angle. The commercial Gaertner Ellipsometric Measurement Program (Version 8.071) was utilized to calculate the layer thickness from the average refractive index determined through ellipsometric measurements at ten different positions on the stainless-steel sample.

During the multilayer formation process, each layer's hydrophobicity was determined by measuring the water contact angle. Static contact angle measurements between the stainless-steel surfaces (1 cm × 1 cm) and water droplets were performed using the Attension Theta tensiometer (Biolin Scientific AB, Gothenburg, Sweden) via the sessile-drop technique. A water droplet (5 μL) was dispensed from a 0.4 mm diameter needle onto the surface, and the static contact angle was measured.

Streaming potential measurements of the coated surfaces were conducted using a SurPASS electrokinetic analyzer (Anton Paar GmbH, Graz, Austria) in a 1 mmol L^{-1} KCl solution at room temperature and pH 6.[43]

The topography and roughness of the uncoated and coated stainless-steel surfaces were analyzed by AFM at room temperature using the Multimode 8 AFM (Bruker, Billerica, MA, USA) in tapping mode with NCHV-A probes (117 μm length, 33 μm width, resonance frequency ∼320 kHz, nominal spring constant 40 N m^{-1}). AFM scans were conducted over a 5 × 5 μm^2 area with a scanning rate of 1 Hz and a picture resolution of 512 × 512 px^2. NanoScope Scan 9.7 was used for data processing, correcting AFM images for tilt and bow using second-order flattening, and NanoScope Analysis 2.0 software was utilized to determine the local root-mean-square (RMS) roughness of LbL films. AFM roughness (RMS roughness, R_q) parameters and their standard deviations were calculated from measurements involving five local areas on each sample surface.

For ion release studies, stainless-steel plates were covered with 2 mL of water and incubated at room temperature for 24 h. The solution above the stainless-steel plates was collected, and the released Zn^{2+} and Cu^{2+} ions were measured using inductively coupled plasma optical emission spectrometry (ICP-OES) on a 5110 ICP-OES (Agilent Switzerland AG, Basel, Switzerland) apparatus. Before measurement, collected solutions were spiked with 2 mL of 4% HNO_3.

2.5. Antibacterial Studies. The bacterial culture was prepared by transferring a colony of *Escherichia coli* DSM 1576 (*E. coli*) into 5 mL of a solution containing 0.25 wt % glucose and 30 wt % Tryptic Soy Broth (TSB, Sigma-Aldrich). The prepared suspension was incubated overnight at 37 °C under shaking (160 rpm). The optical density of the overnight bacterial culture was measured at 600 nm, and the culture was diluted to 0.10 optical density in 5 mL of fresh 30 wt % TSB supplemented with 0.25 wt % glucose. The diluted suspension was regrown for 2 h at 37 °C with shaking (160 rpm) to achieve exponential cell growth. The *E. coli* suspension was further diluted in 0.9% NaCl to 0.01 optical density at 600 nm, corresponding to ≈10^5 colony-forming units (CFU).

The sterilized stainless-steel samples (1 × 1 cm) were placed in a 24-well plate. Subsequently, 100 μL of the diluted bacterial suspension (10^5 CFU) was added to each sample and incubated for 24 h at room temperature. After incubation, the stainless-steel samples were washed twice with 1 mL of 0.9% NaCl solution, and the washing solution was used for agar spotting after dilution. Washed stainless-steel samples were placed into 2.5 mL of 0.9% NaCl solution and

https://doi.org/10.1021/acsanm.4c00981
ACS Appl. Nano Mater. XXXX, XXX, XXX−XXX

sonicated in a sonication water bath for 5 min, followed by 15 s of vigorous vortexing at the highest speed. After a series of dilutions, 20 μL of the *E. coli* suspension was plated on plate count agar plates and incubated at 37 °C for 18 h to enumerate planktonic and adherent cells. The total viable cells were expressed as a sum of planktonic and adherent cells.

To determine the coating antibacterial efficiency the percentage reduction in the viable bacteria was calculated from Equation 1:

$$P = \left(1 - \frac{B}{A}\right) \times 100 \quad (1)$$

by using the number of viable bacteria before coating (A) and the number of viable bacteria after the coating application (B).

2.6. Biocompatibility Evaluation. Immortalized human keratinocytes HaCaT (ATCC, Manassas, Virginia, USA) were used for cytotoxicity experiments following ISO 10993−5 norm. Cells were cultured until 80% confluence in 10 mL high glucose Dulbecco's Modified Eagle Medium (DMEM) supplemented with 10% (HI) FBS, 1% Penicillin/Streptomycin, and 1% Non-Essential-Amino-Acids (all obtained from Gibco, Life Technologies Corporation, Painsley, United Kingdom) at 37 °C and 5% CO_2. The culture medium was then removed. Cells were rinsed once with sterile PBS, detached from the flask by adding 1 mL of 0.25% Trypsin-EDTA solution (Sigma-Aldrich, St. Louis, Missouri, USA), and incubated at 37 °C and 5% CO_2 for 10 min. Detached cells were counted on a TC20 automated cell counter (Biorad, Hercules, California, USA). Cells were then seeded in sterile 96-well plates (Thermo Fisher Scientific, Waltham, Massachusetts, USA) with a seeding density of 20,000 cells/well for assays with a microplate reader.

The stainless-steel plates were covered with 1 mL of serum-free DMEM and incubated at room temperature for 24 h under shaking (50 rpm). The solution above stainless-steel plates was collected and used for further experiments. The cells adhered to the 96-well plates were washed with PBS, covered with 100 μL of the solution from the stainless-steel samples, and incubated for 4 h. In the experiment, the clean stainless-steel plate solution was the negative control, and cells treated with Triton-X 1% were the positive control. After incubation, the cells were washed three times with PBS and covered with 100 μL of media and 20 μL of CellTiter 96 AQueous One Solution Cell Proliferation Assay (MTS) (Promega, Madison, Wisconsin, SAD) and incubated for 3 h. Afterward, the absorbance at 490 nm was measured using a Clariostar plate reader (BMG LABTECH GmbH, Ortenberg, Germany).

2.7. Statistical Analysis. All experiments were conducted in triplicate. Statistical analysis was performed using the Tukey test (GraphPad Prism 8, La Jolla, CA, USA) and three-way analysis of variance (ANOVA) to evaluate the significance of NP type, polyelectrolyte type, and NP morphology, with significance levels set at * $p \leq 0.05$, ** $p \leq 0.01$, *** $p \leq 0.001$, and **** $p \leq 0.0001$. Statistical significance was considered for the p-value below 0.05, i.e., 95% of the confidence interval.

3. RESULTS AND DISCUSSION

3.1. Synthesis of CuO and ZnO Nanoparticles. Nanoparticles (NPs) with various morphologies were synthesized under different conditions, including NaOH concentration, temperature, and reaction time variations. Subsequently, the obtained NPs were annealed and subjected to analysis using FTIR and XRD techniques to validate their composition (Figure 1). The FTIR spectrum of CuO samples (Figure 1A) shows distinct metal oxide vibrations at the following wavenumbers (ν/cm^{-1}): 404 cm^{-1}, 483 cm^{-1}, and 610 cm^{-1}, which can be attributed to Cu−O symmetric stretching, asymmetric stretching, and wagging, respectively.[44] The ZnO spectra (Figure 1A) showed symmetric Zn−O stretching vibration at 353 cm^{-1}.[45] Notably, neither CuO nor

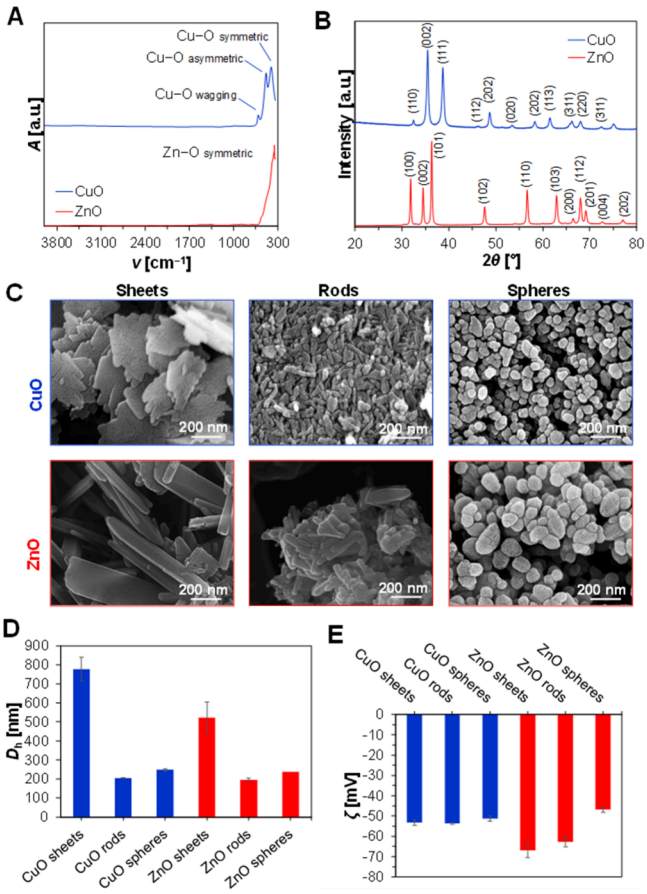

Figure 1. Characterization of CuO and ZnO NPs. (A) Representative Fourier transformed infrared spectra showing the sample absorbance (A) at specific wavenumber (ν/cm^{-1}) with indicated bond vibrations and (B) X-ray diffraction intensity of CuO and ZnO NPs at specific 2θ angles with assigned (hkl) crystallographic planes. (C) Scanning electron microscopy images of prepared CuO (first row, blue) and ZnO (second row, red) exhibiting sheet- (first column), rod- (second column) and sphere-like (third column) morphology. (D) Hydrodynamic diameter (D_h) and (E) zeta potential (ζ) of CuO and ZnO NPs with different morphology (sheets, rods, and spheres) dispersed in water at neutral pH.

ZnO spectra showed any residual OH groups from the synthesis process.

XRD analysis confirmed the purity and crystalline nature of the annealed NPs, revealing characteristic diffraction peaks for CuO and ZnO (Figure 1B). The CuO diffractogram exhibited peaks at angles 2θ 32.5°, 35.4°, 38.7°, 48.7°, 53.4°, 58.2°, 61.5°, 66.2°, 68.0°, 72.4°, and 75.1° corresponding to crystallographic planes (hkl) (110), (002), (111), (112), ($\bar{1}$02), (020), (20$\bar{2}$), (113), ($\bar{3}$11), (220), (311), and (004), respectively, as confirmed by JCPDS card number 80−1917. The XRD pattern corresponded to the monoclinic CuO phase. Similarly, characteristic diffractions of ZnO powder were observed at angles 2θ 31.8°, 34.4°, 34.3°, 47.5°, 56.6°, 62.8°, 66.4°, 68.0°, 70.0°, 72.6° and 76.9° corresponding to crystallographic planes (hkl) (100), (002), (101), (102), (110), (103), (200), (112), (201), (004) and (202), respectively, validated by JCPDS card number 36−1451.

SEM micrographs revealed various CuO and ZnO NPs morphologies, including sheet-, rod- and sphere-like structures (Figure 1C). CuO sheet-like[26] NPs displayed irregular morphology with rugged, uneven edges, with an average size

https://doi.org/10.1021/acsanm.4c00981
ACS Appl. Nano Mater. XXXX, XXX, XXX−XXX

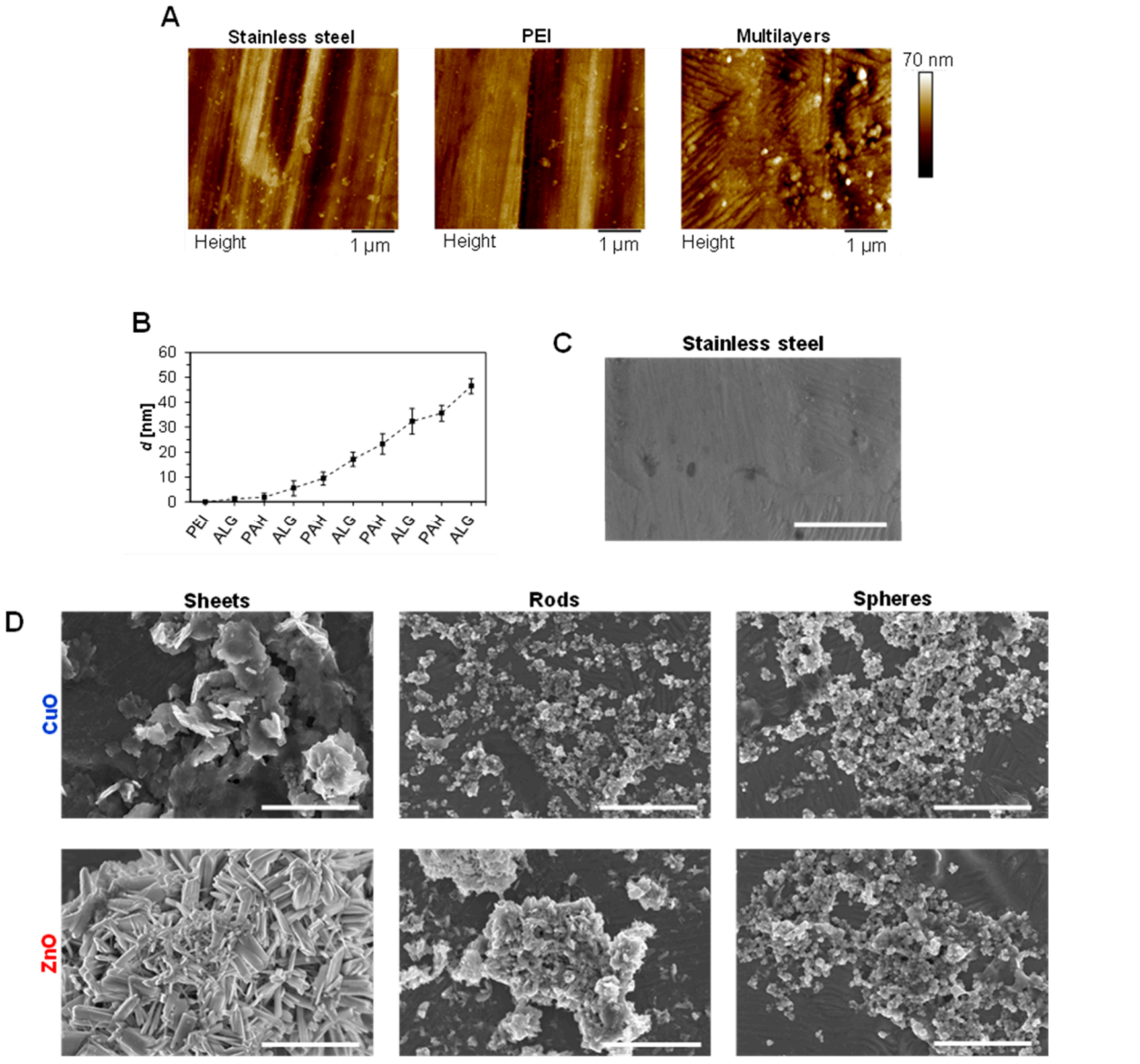

Figure 2. Characterization of stainless-steel surface after the application of multilayers. (A) AFM images of pure stainless-steel surface, surface with a single layer of PEI, and polyelectrolyte multilayers without NPs. (B) The thickness (d) of each polyelectrolyte layer applied, with PEI as the first precursor layer, followed by PAH/ALG layers. The dashed line is added to guide the eye. Scanning electron microscopy images of (C) uncoated stainless-steel surface and (D) stainless-steel surface coated with PAH/ALG multilayers and CuO (first row, blue) and ZnO (second row, red) exhibiting sheet- (first column), rod- (second column) and sphere-like (third column) morphology. The scale bar is 2 μm. PEI − poly(ethylenimine); ALG − alginate; PAH − poly(allylamine hydrochloride).

of (434.0 ± 118.5) nm. Conversely, ZnO sheet-like NPs exhibited more rectangular shapes with elongated morphology, well-defined edges, and an average size of (630.4 ± 154.8) nm. CuO and ZnO[27] rod-like NPs displayed elongated morphologies with slightly different sizes, namely (63.4 ± 16.2) nm and (91.7 ± 27.9) nm, respectively. Sphere-like CuO and ZnO NPs demonstrated similar sizes, with (59.8 ± 11.8) nm and (62.4 ± 16.7) nm, respectively.

Furthermore, in the case of rod- and sphere-like NPs, the hydrodynamic diameter of CuO and ZnO NPs was similar (Figure 1D). Rod-like CuO and ZnO NPs exhibited a hydrodynamic diameter of approximately 200 nm, while the sphere-like structures showed a slightly bigger hydrodynamic diameter of ≈240 nm. In contrast, sheet-like NPs displayed larger hydrodynamic diameters, measuring (777 ± 62) nm for CuO and (522 ± 81) nm for ZnO NPs. The hydrodynamic diameter of the sheet-like NPs was determined with the approximation for spherical particles, and the exact size of the NPs was determined by analyzing the SEM images as shown above.

The specific surface area analysis indicated distinct values for different morphologies of CuO and ZnO NPs. CuO NPs exhibited surface areas of 16.5 $m^2\ g^{-1}$ for sheet-, 19.4 $m^2\ g^{-1}$ for rod-, and 13.4 $m^2\ g^{-1}$ for sphere-like CuO NPs. Similarly, ZnO NPs displayed surface areas of 5.9 $m^2\ g^{-1}$ for sheet-, 18.2 $m^2\ g^{-1}$ for rod-, and 11.1 $m^2\ g^{-1}$ for sphere-like structures. The difference in the specific surface area between CuO and ZnO sheet-like NPs can be explained by the difference in the surface profile of the NPs. The surface of CuO NPs showed expressed roughness in the form of cracks and cuts that were not visible on ZnO crystals, contributing to the higher surface area of CuO NPs. Also, ZnO NPs were approximately 200 nm bigger

https://doi.org/10.1021/acsanm.4c00981
ACS Appl. Nano Mater. XXXX, XXX, XXX−XXX

than CuO NPs, which also contributes to the smaller specific surface area of ZnO NPs.[46]

Different morphologies of CuO and ZnO NPs were achieved by manipulating preparation conditions, such as NaOH concentration, temperature, and reaction time. Notably, this approach facilitated the generation of diverse NPs sharing similar size and morphology, excluding the influence of these parameters on antibacterial activity or other properties among NPs with distinct chemical compositions. Notably, the NPs were synthesized without the addition of directing molecules, which are known to shape specific morphological features, as shown for spherical flowers prepared with the addition of cetyltrimethylammonium bromide,[47] nano pellets and various spheres prepared with biological plant extracts.[20,21,48] The exclusion of such molecules eliminates potential alterations in antibacterial properties, focusing solely on the influence of NP chemical composition between CuO and ZnO.

All types of CuO and ZnO NPs showed a negative zeta potential (at pH ≈ 7) (Figure 1E). The zeta potential was similar among CuO sheets, rods, spheres, and ZnO spheres (≈ − 50 mV), whereas it was more negative for ZnO sheets and rods (≈ − 64 mV). The negatively charged NPs (at pH ≈ 7) were immobilized between positively charged PAH polyelectrolyte layers on the stainless-steel surfaces.

3.2. Coating Characterization. To corroborate the formation of the polyelectrolyte multilayers on the stainless-steel surfaces, atomic force microscopy (AFM) was employed to visualize surface morphology and roughness. The morphology of the uncoated stainless-steel was characterized by linear lines extending in the polishing direction and small grain-like structures on the surface (Figures 2A and 2C). The specific surface profiles can be attributed to the mechanical polishing used to smooth out the substrate surface,[49] and the grain-like structures are, most likely, the residue of the materials used in the polishing process.

The surface was pretreated with one PEI layer before applying the PAH/ALG polyelectrolyte layers. PEI served as a precursor layer to enhance polyelectrolyte layer binding to the stainless-steel surface, leading to significantly thicker layers, as Nikolić et al. demonstrated.[50] The addition of a single layer of PEI did not significantly alter the surface morphology or roughness, indicating minimal impact with surface roughness parameters, R_q, being (8.8 ± 0.4) nm and (8.0 ± 0.6) nm for uncoated and PEI-coated stainless-steel surface, respectively.

Following PAH/ALG multilayer formation, as depicted in Figure 2A, a notable change in surface morphology, observed as rod- and grain-like structures, along with a slight increase in surface roughness to (10.6 ± 1.1) nm, indicated successful polyelectrolyte multilayer deposition. Additionally, ellipsometry measurements confirmed PAH/ALG multilayer formation on the stainless-steel surface. Figure 2B shows the exponential growth of multilayer thickness, resulting in a film thickness of (46.5 ± 3.0) nm upon completion of layer deposition.

Whereas the increase in surface roughness was noticed between the uncoated and PAH/ALG coated stainless-steel, it can still be primarily attributed to the roughness of the substrate and not the polyelectrolyte multilayer itself, as the multilayer is adsorbed into the lines and cracks caused by the polishing process as well as the smoother parts of the surface. Bohinc et al. previously demonstrated a positive correlation between surface roughness and the adhesion rate of bacteria. Their findings suggested that the heightened adhesion could be attributed to the amplified interaction between the expanding effective surface area and the augmented presence of cracks, voids, and crevices.[51] However, the influence of surface roughness on bacterial adhesion can be neglected in this study due to the extremely small difference in the surface roughness of the bare stainless steel and the PAH/ALG coated one. Nonetheless, it is necessary to consider other properties of the surface that can affect the binding of bacteria due to PAH/ALG coating.

The CuO and ZnO NPs agglomerate on the PAH/ALG multilayers during the drying process and form a network of NP islands on the surface of the stainless-steel (Figure 2D). The EDS mapping (Figures S1, S2) confirmed the composition of the NP islands on the stainless-steel surface. Moreover, the FTIR spectra of PAH/ALG multilayers containing CuO NPs (Figures 3A, S3) showed, in the case of CuO sheets, a shift of the CuO peaks to 424 cm^{-1}, 500 cm^{-1}, and 612 cm^{-1} and in the case of CuO rods and spheres to 442 cm^{-1}, 534 cm^{-1}, and 600 cm^{-1}. Additional peaks at 1009 cm^{-1}, 1035 cm^{-1}, 1128 cm^{-1}, 1400 cm^{-1} and 1600 cm^{-1} were observed which were not present in the FTIR spectra of pure CuO NPs. FTIR spectra of PAH/ALG multilayers containing ZnO NPs (Figures 3B, S4) showed a shift of the ZnO peaks to a broad peak at 498 cm^{-1}. Additional peaks at 1006 cm^{-1}, 1036 cm^{-1}, 1128 cm^{-1}, and 1400 cm^{-1} were observed which were not present in the FTIR spectra of pure ZnO NPs. The observed shift of the CuO and ZnO peaks can be attributed to the presence of the PAH/ALG multilayers especially due to ALG which exhibits a peak at 612 cm^{-1} and a broad absorption area below 570 cm^{-1}. In the ALG spectra specific peaks at 1593 cm^{-1} and 1408 cm^{-1} were attributed to the asymmetric and symmetric stretching vibrations of carboxylate, while the peaks at 1025 cm^{-1} and 949 cm^{-1} were attributed to pyranose ring C−O stretching vibration and C−C−H and C−O−H deformation.[52] The PAH spectra exhibited specific peaks at 1602 cm^{-1} and 1507 cm^{-1} attributed to vibrations of the amide group.[53] The FTIR analysis confirmed the presence of both NPs and polyelectrolytes on the surface of the stainless-steel substrate. XRD analysis of the stainless-steel plates with PAH/ALG multilayers and NPs showed specific diffraction peaks at 43.52°, 50.66° and 74.47° corresponding to the stainless-steel and diffraction peaks corresponding to ZnO and CuO NPs (Figure 3C).

Water contact angle measurements showed that uncoated stainless-steel surfaces exhibited hydrophilic characteristics (Figure 4A). The water contact angle of pure stainless-steel was (80.7 ± 4.8)°. After applying the PEI layer, the surface hydrophobicity did not change noticeably. However, subsequent application of PAH/ALG layers decreased the water contact angle by 10° and 20°, respectively. The highest decrease in hydrophobicity occurred after sheet-, rod-, and sphere-like NP application ($CA \approx 40°$) (Figure 4 B, C, and D). No significant differences regarding the contact angle were observed for the NP layers, regardless of the NP morphology or chemical composition (CuO/ZnO).

Since bacteria interact and adhere to surfaces, it is essential to determine the properties of the PAH/ALG-terminating multilayer. The water contact angle of the terminating applied layers was higher for the PAH layer (≈ 63°) than the ALG layer (≈ 45°), which could affect the interaction between the surfaces and the bacterial cell. Numerous studies have shown that bacteria whose surface properties are hydrophilic adhered more significantly to hydrophilic surfaces.[54−57] Hamadi et al.

https://doi.org/10.1021/acsanm.4c00981
ACS Appl. Nano Mater. XXXX, XXX, XXX−XXX

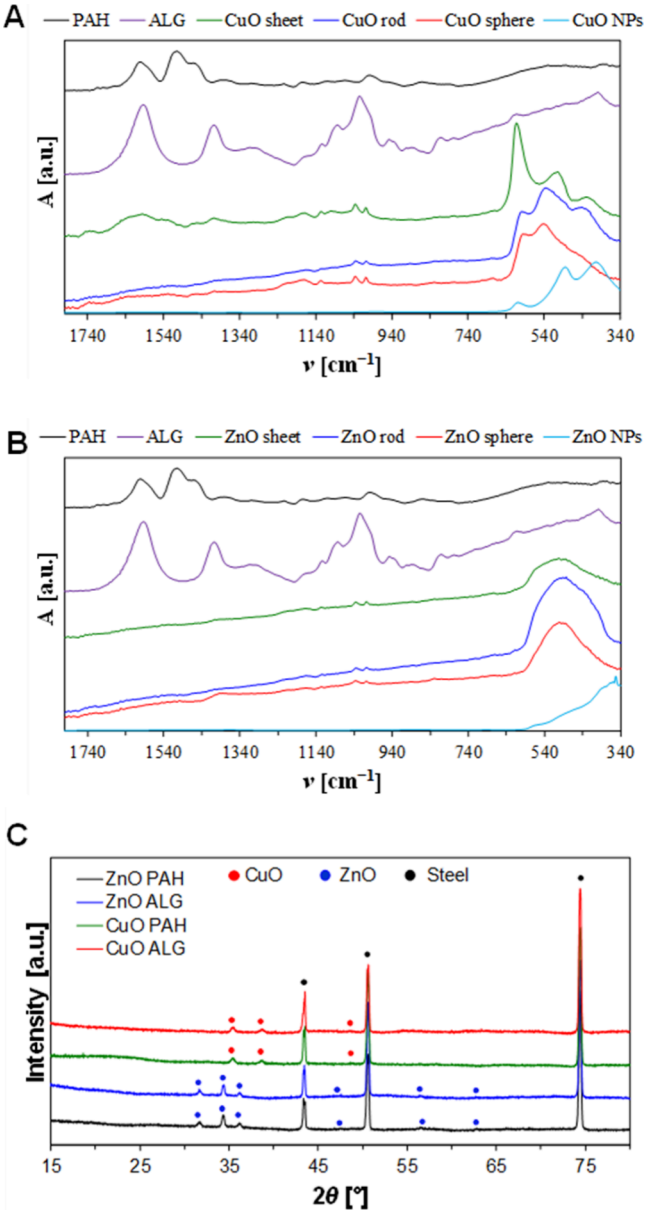

Figure 3. Representative Fourier transformed infrared spectra showing the absorbance (A) at specific wavenumber (ν/cm^{-1}) for alginate and poly(allylamine hydrochloride) powders and stainless-steel plates coated with ALG terminating multilayers containing (A) CuO and (B) ZnO NPs. (C) Representative X-ray diffractograms of stainless-steel plates after application of PAH/ALG multilayers with CuO and ZnO NPs at specific 2θ angles. PAH − poly(allylamine hydrochloride), ALG - alginate

studied three strains of *E. coli* and showed that they are characterized by hydrophilic properties with an average water contact angle of 23°.[58] Due to the hydrophilic characteristics of bacteria, they are expected to adhere to PAH/ALG-coated stainless steel surfaces.

The surface charge is another property that can influence the adhesion of bacteria. Zeta potential analysis of uncoated stainless-steel (Figure 5) revealed that the solution pH change from 6 to 9 decreased surface zeta potential from −30 mV to −60 mV. After coating, the surfaces with PAH as a terminating layer exhibited positive zeta potential (Figure 5B). In contrast, surfaces with ALG as the terminating layer displayed negative zeta potential (Figure 5C), regardless of the type of NPs used. Surface charge influences bacterial adhesion, where negatively charged bacteria are more attracted to positively charged surfaces. Kozmos et al. demonstrated that negatively charged surfaces are more repulsive to the adhesion of negatively charged bacteria, leading to lower bacterial adhesion extent.[59]

3.3. Ion Release. Polyelectrolyte layers were utilized to encapsulate NPs, reducing direct contact with human cells and preventing NP release from the stainless-steel surface while facilitating the release of Cu^{2+} and Zn^{2+} ions for antibacterial action. ICP analysis showed that no free NPs were observed after 24 h of incubation in water, indicating effective NP attachment to the stainless-steel surface. Conversely, the release of Cu^{2+} and Zn^{2+} ions into the water solution was observed (Figure 6). The determined Zn^{2+} concentrations were higher (1.0 to 2.5 mg/L) compared to Cu^{2+} (below 0.5 mg/L), regardless of the terminating polyelectrolyte layer.

3.4. Antibacterial Activity. The antibacterial tests were conducted on the *E. coli* DSM 1576 strain. Figure 7 depicts the number of planktonic and adhered *E. coli* on stainless-steel surfaces coated with different terminating polyelectrolyte multilayers containing embedded NPs. The number of planktonic cells exposed to surfaces coated solely with polyelectrolyte multilayers without added NPs (log(CFU/mL) = 5.4 ± 1.2) did not significantly differ from bare stainless-steel (log(CFU/mL) = 6.1 ± 0.4). The reduction in viable *E. coli* cells (Table 2) for the PAH terminating layer was (53.0 ± 28.2)% and (60.6 ± 53.9)% for the ALG terminating layer which could not be considered significant for bacterial eradication. Despite previous literature suggesting the antibacterial properties of poly(allylamine hydrochloride),[29,60,61] the prepared polyelectrolyte layers did not exhibit a significant antibacterial effect against the tested *E. coli* strain. The discrepancy could be caused by the different test conditions and/or bacterial strains used here and in the previous work.

The application of NPs resulted in decreased viable planktonic cells (Figure 7, Table 2). ZnO NPs notably reduced the number of viable planktonic *E. coli* (Table 2), especially with ALG as the terminating layer, where no viable cells were observed (100% reduction in cell viability). CuO NPs showed a decrease in viable planktonic *E. coli* on ALG surfaces exceeding 99.8%, and no statistically significant decrease on PAH surfaces ($p > 0.5$).

Regarding adhered bacterial cells, the viability of the *E. coli* cells on the surfaces coated with PAH terminating layers without NPs was reduced by (47.4 ± 26.8)%, which could not be considered significant for bacterial eradication. For the ALG terminating layers, the reduction of the viability was not observed (Figure 7, Table 2). However, upon ZnO and CuO NP addition, no viable *E. coli* cells were determined on the surfaces (100% reduction in cell viability), regardless of NP morphology or terminating polyelectrolyte layer.

The total number of viable cells (planktonic and adhered) was assessed to evaluate the overall effect of NP morphology and polyelectrolyte layers (Figure 7). Three-way analysis of variance (ANOVA) was used to test the statistical differences among NP morphology, composition (CuO and ZnO), and terminating multilayer type (PAH/ALG) regarding the viability of *E. coli* cells. Results indicated no statistically significant variations between terminating multilayer types (p = 0.4972). Both NP morphology (p = 0.0001) and composition (p = 0.0101) significantly affected the viability of *E. coli* cells. Furthermore, no notable interaction occurred between

https://doi.org/10.1021/acsanm.4c00981
ACS Appl. Nano Mater. XXXX, XXX, XXX−XXX

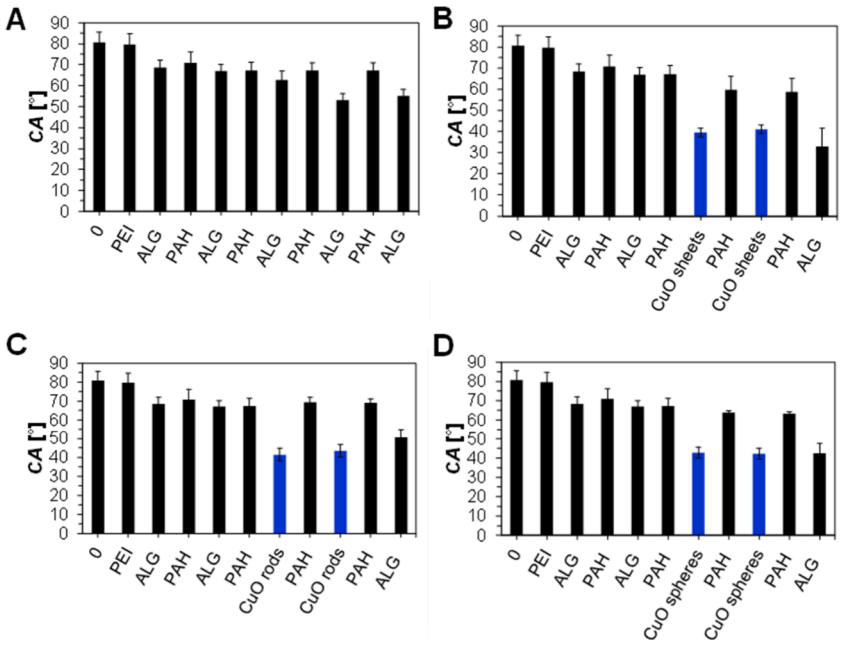

Figure 4. Water contact angle (*CA*) on bare stainless-steel surface (A) and stainless-steel surface coated with polyelectrolyte multilayers and sheet- (B), rod- (C), and sphere-like CuO NPs (D). The water contact angle of ZnO layers exhibited similar contact angles to those of CuO NPs and are not shown here. PEI – poly(ethylenimine); ALG – alginate; PAH – poly(allylamine hydrochloride).

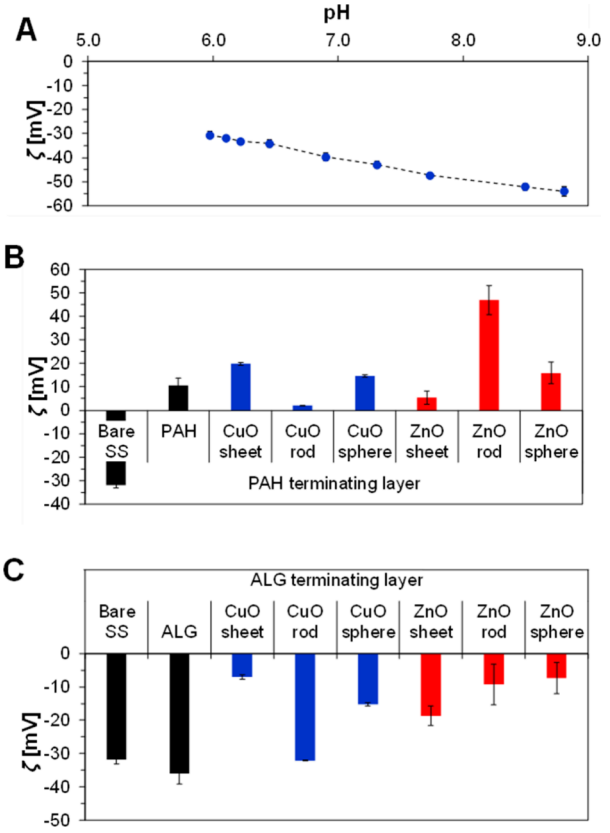

Figure 5. Surface zeta potential (ζ) of (A) bare stainless-steel at different pH, where the line is added to guide the eye. Zeta potential of samples coated with PAH (B) and ALG (C) as terminating polyelectrolyte layers, with CuO and ZnO NPs at pH = 6. SS – stainless-steel; poly–polyelectrolyte multilayers without NPs; ALG – alginate; PAH – poly(allylamine hydrochloride).

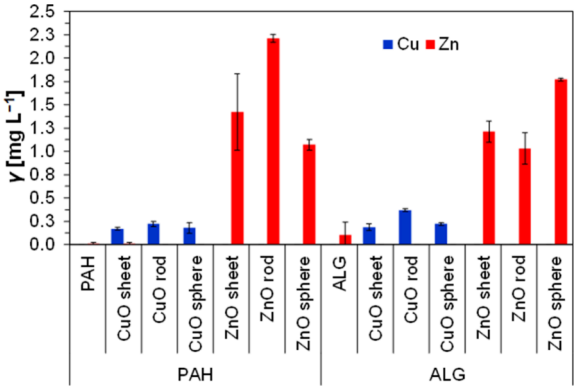

Figure 6. ICP-OES analysis of released Cu^{2+} and Zn^{2+} ions from the stainless-steel surface coated with NPs and PAH or ALG as terminating polyelectrolyte layer. ALG – alginate; PAH – poly(allylamine hydrochloride).

pairwise comparisons between all three parameters (p > 0.2206).

Statistical analysis revealed that ZnO NPs exhibit a more pronounced antibacterial effect against *E. coli* than similar-sized and shaped CuO NPs. Notably, rod-like ZnO NPs displayed the highest antibacterial activity among different morphologies. In the case of CuO, morphology's influence was less apparent. Between ZnO NPs, rod-like structures exhibited the highest surface area (18.2 m^2 g^{-1}), correlating with increased antibacterial effectiveness. Smaller NPs with higher surface area are more easily dissolved.[62,63] Although CuO rod-like NPs exhibited a similar surface area (19.4 m^2 g^{-1}) to ZnO NPs, their antibacterial activity against planktonic *E. coli* was minimal. ICP-OES analysis (Figure 6) revealed that surfaces with ZnO NPs released up to ten times higher ion concentrations than CuO NPs, explaining the difference in antibacterial activity. Previous studies[22,23] also demonstrated better antibacterial performance of ZnO compared to CuO.

https://doi.org/10.1021/acsanm.4c00981
ACS Appl. Nano Mater. XXXX, XXX, XXX−XXX

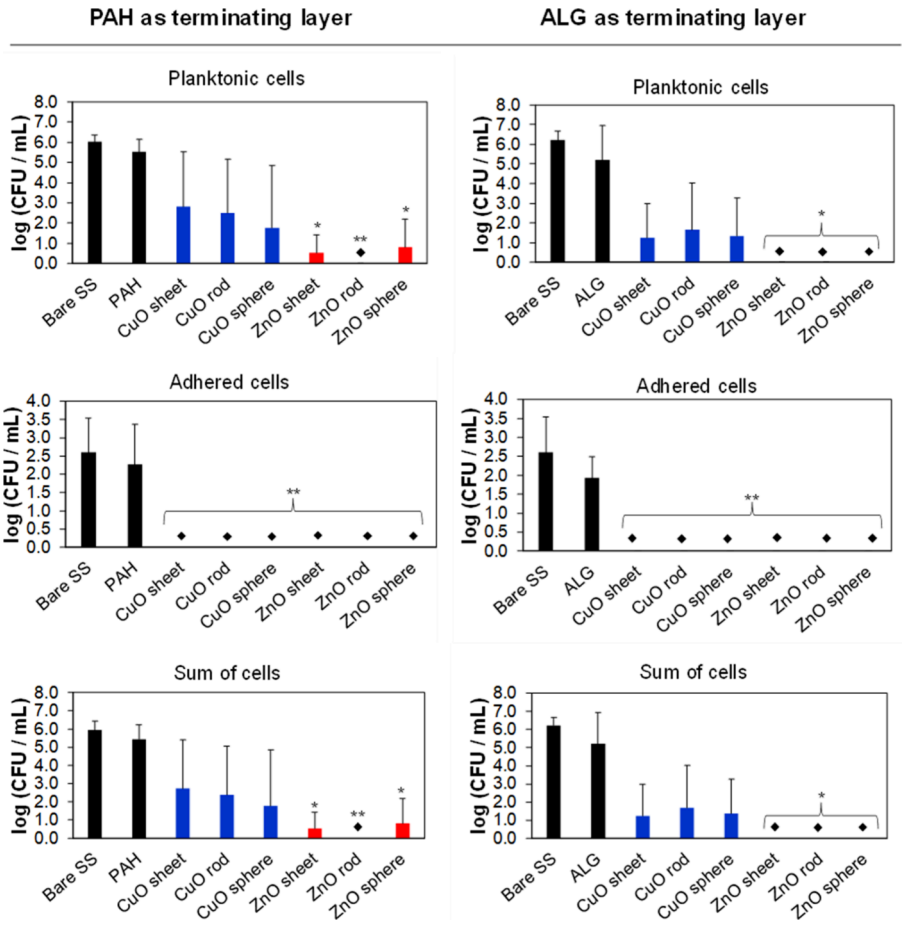

Figure 7. Average bacteria count per milliliter (CFU/mL) on stainless-steel surfaces coated with ZnO and CuO NPs against Gram-negative *Escherichia coli* (*E. coli*). The number of planktonic and adhered cells and the sum of bacterial cells are shown for polyelectrolyte multilayers with PAH (left column) or ALG (right column) as the terminating layer. Significance was determined using a three-way ANOVA Tukey test of the log reduction data points compared to uncoated stainless-steel surfaces with * $p \leq 0.05$ and ** $p \leq 0.01$. SS − stainless-steel; ALG − alginate; PAH − poly(allylamine hydrochloride).

Table 2. Percentage Reduction (P) in Planktonic and Adhered *Escherichia coli* (*E. coli*) Viability on the PAH/ALG Multilayers with CuO and ZnO Nanoparticles[a]

	Planktonic *E. coli*		Adhered *E.coli*	
	P (PAH terminating layer) [%]	P (ALG terminating layer) [%]	P (PAH terminating layer) [%]	P (ALG terminating layer) [%]
Without NPs	53.0 ± 28.2	60.6 ± 53.9	47.4 ± 26.8	–[b]
ZnO sheet	99.9 ± 0	100 ± 0	100 ± 0	100 ± 0
ZnO sphere	99.9 ± 0	100 ± 0	100 ± 0	100 ± 0
ZnO rod	100 ± 0	100 ± 0	100 ± 0	100 ± 0
CuO sheet	90.8 ± 13.0	99.9 ± 0	100 ± 0	100 ± 0
CuO sphere	91.7 ± 11.7	99.9 ± 0.1	100 ± 0	100 ± 0
CuO rod	92.6 ± 10.5	99.9 ± 0.2	100 ± 0	100 ± 0

[a]PAH − poly(allylamine hydrochloride), ALG − alginate. [b]− no reduction in cell viability.

For instance, Ginjupalli et al. used commercial CuO and ZnO sphere-like NPs in alginate dental impression materials. They observed antibacterial activity against *E. coli* for ZnO at NP concentrations (up to 5 wt %).[64] However, they did not explore cytotoxicity at the studied concentrations.

3.5. Biocompatibility Experiments. The biocompatibility of coated stainless-steel surfaces was investigated *in vitro* on immortalized human keratinocytes (HaCaT) cells. The potential toxicity of the released Zn^{2+} and Cu^{2+} ions on the HaCaT cells was evaluated by indirect assay. Cell viability was determined by observing the change of metabolic activity with respect to the cells grown in the supernatant collected after incubation on pure stainless-steel plates. The metabolic activity (Figure 8) showed no statistically significant decrease in the cells' viability compared to the noncoated materials (as control specimens; $p > 0.05$), regardless of the NP type, morphology, or the type of the terminating polyelectrolyte layer. Three-way analysis of variance (ANOVA) was used to test the statistical differences among NP morphology, composition (CuO and ZnO), and terminating multilayer type (PAH/ALG) regarding the viability of HaCaT cells. Results indicated no statistically significant variations in NP composition ($p = 0.1978$). Nevertheless, both NP morphology and terminating multilayer affected the cytocompatibility ($p < 0.0007$) (Figure 8A). Moreover, notable interaction occurred between pairwise comparisons of NP morphology and composition ($p = 0.0001$), NP morphology and terminating multilayer type ($p = 0.0017$), and NP composition and terminating multilayer type ($p = 0.0007$). Even though the ICP-OES results (Figure 6) show that ZnO NPs (up to 2.5 mg/L) release significantly

https://doi.org/10.1021/acsanm.4c00981
ACS Appl. Nano Mater. XXXX, XXX, XXX−XXX

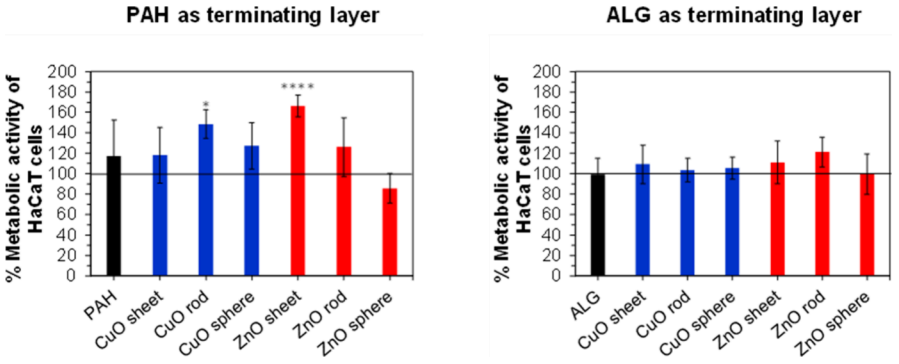

Figure 8. Metabolic activity of HaCaT cells on the stainless-steel surface coated with PAH (left column) or ALG (right column) as the terminating multilayer containing embedded NPs. The presented results are relative to the uncoated stainless-steel surface. Significance was determined using a three-way ANOVA Tukey test with * $p = 0.0101$ and **** $p \leq 0.0001$. ALG − alginate; PAH − poly(allylamine hydrochloride).

higher ion concentrations than CuO NPs (below 0.5 mg/L), the cytotoxicity on HaCaT cells was not observed. The surfaces coated with NPs and PAH as the terminating layer enhanced cells' viability, compared to the stainless-steel surface coated solely with polyelectrolyte multilayers, especially the samples with ZnO sheets ($p \leq 0.0001$) and CuO rods ($p = 0.0101$) (Figure 8). No enhancement in the cell viability was observed in the samples with ALG as the terminating polyelectrolyte layer (Figure 8). Compared to other research,[64] we used low concentrations of CuO and ZnO NPs (V_{total} = 200 μL, γ(NPs) = 115 μg/mL) and showed good antibacterial activity. Previously, we have shown that orthotic materials treated with CuO NPs show good antibacterial activity against Gram-positive bacteria but also cause cytotoxic effects on human cells.[26] To limit the cytotoxicity of the NPs, we used polyelectrolyte multilayers to immobilize the NPs, hence reducing the release of NPs and Cu^{2+} and Zn^{2+} ions. The cytotoxicity of the surfaces was not observed. Based on the literature data, the toxicity of NPs is much higher than that of the dissolved ions[25] and different approaches such as surface modification, size, and route of exposure can minimize the toxic effect[65] so the immobilization of NPs in polyelectrolyte layers is an excellent approach to limit their toxicity. Zn^{2+} and Cu^{2+} ions play pivotal roles in cellular pathways, facilitating normal cell functions, and at low ion concentrations, they are beneficial for cell viability.[66] However, high Zn^{2+} and Cu^{2+} ion concentrations can induce toxicity and cellular death through diverse mechanisms. Cu^{2+} ions, for instance, are known to impair cell membranes, induce oxidative stress, and affect intercellular proteins and nucleic acids.[67−69] Conversely, Zn^{2+} ions inactivate bacterial cells through the intracellular generation of reactive oxygen species, subsequently leading to damage of biomolecules.[70−72] Unlike Cu^{2+} ions, Zn^{2+} ions do not typically instigate membrane degradation and disruption. Instead, they induce higher membrane permeability, rendering the cell more susceptible to the action of NPs.[66] It is important to note that in this study, the NPs are added between polyelectrolyte layers, thereby diverging from the direct interaction with the cell membrane. Previously, we explored the change in metabolic activity of HaCaT cells at Zn^{2+} ion concentrations ranging from 0.5 μg mL^{-1} to 20 μg mL^{-1}.[27] The metabolic activity results revealed no statistically significant decrease in cell viability up to 7 μg mL^{-1} of Zn^{2+} ions compared to the control specimen without Zn^{2+} ions. Also, the viability of HaCaT cells slightly increased for low concentrations of Zn^{2+} ions: 0.5 μg mL^{-1} to (102.5 ± 8.1)%, 1 μg mL^{-1} to (103.6 ± 4.5)% and 3 μg mL^{-1} to (100.3 ± 7.0)%.[27] This shows that the viability of HaCaT cells in media with up to 3 μg mL^{-1} of Zn^{2+} ions does not differ significantly so the influence of the ions (Figure 6) could be disregarded when comparing PAH and ALG terminating layers. Both PAH and ALG are biocompatible materials as shown by a wide variety of research.[32,33,73−76] As the cytocompatibility experiments show, the surfaces coated with PAH terminating layer demonstrate a higher average increase of HaCaT metabolic activity of (117.0 ± 35.9)%, compared to the uncoated stainless-steel surface, than the surfaces with ALG terminating layer (99.1 ± 15.9)%. The results indicate a slightly higher increase in cytocompatibility of surfaces coated with the PAH terminating layer than the one with the ALG terminating layer which could explain the overall difference. Literature shows that alginate can enhance cell viability[33] but in the research we conducted the enhancement was not noticed.

Overall, the antibacterial results indicate that despite similar size, morphology, and surface area, differences in chemical composition and solubility among NPs play a pivotal role in antibacterial activity. Regarding polyelectrolyte layers, complete inhibition of bacterial growth was observed on surfaces with ZnO NPs and ALG as the terminating layer. Surface roughness did not change significantly after PAH/ALG NP application, but hydrophobicity (Figure 4) and zeta potential (Figures 5 B and C) are crucial factors. The bacteria are expected to adhere to more hydrophilic layers since higher bacterial adhesion is achieved between bacterial cells and surfaces with similar hydrophobicity, i.e., hydrophilicity.[54−56,77] A smaller contact angle was measured for the ALG- (≈ 45°) and a larger one for the PAH- (≈ 63°) terminating multilayer.

Studies conducted on various *E. coli* strains demonstrated that the bacterial cells exhibit negative surface charge from −3.5 mV to −49 mV.[78−80] Repulsive forces are expected between negatively charged bacterial cells and negatively charged coatings.[30,31] However, with higher ionic strengths used during experiments in the present study, the influence of electrostatic forces decreases due to ion screening, allowing other interactions, such as van der Waals forces and specific chemical interactions, to become more prevalent.[81] At these conditions, the repulsive electrostatic forces between the negatively charged bacteria and negatively charged multilayers could be reduced, potentially enabling bacterial adhesion.[82] Moreover, hydrophobicity contributes to bacterial adhesion to surfaces with ALG as the terminating layer. ALG layers attract bacteria cells more strongly, enabling better adhesion and

https://doi.org/10.1021/acsanm.4c00981
ACS Appl. Nano Mater. XXXX, XXX, XXX−XXX

action of released Zn^{2+} and Cu^{2+} ions, which could explain the noticed antibacterial activity. The results (Figure 7) indicate that CuO NPs might only prevent surface bacteria growth, suggesting CuO may not be optimal for broad applications. It is more convenient to use ALG as terminating layers with ZnO NPs for surface coating since the antibacterial activity is exceptionally high and the biocompatibility is not reduced. The development of antibacterial, and biocompatible coatings using the proposed PAH/ALG multilayers with CuO and ZnO NPs holds promise for diverse applications, especially in healthcare. The application of NPs for antibacterial usage must be conducted in a way the biocompatibility and safety for the user are preserved. The electrostatic attraction forces were used as the primary criteria for the layer-by-layer PAH/ALG development and CuO and ZnO NPs immobilization on the stainless-steel surface. Overall the stainless-steel demonstrated negative zeta potential (Figure 5) from −30 mV to −60 mV ($6 < pH < 9$). The negative stainless-steel surface was treated with a positively charged precursor layer PEI to enhance the polyelectrolyte layer binding to the negatively charged surface.[50] After the application of the precursor layer negatively charged ALG layer was followed by a positively charged PAH layer as described by Xiao et all.[41] The negatively charged CuO and ZnO NPs (Figure 1E) were immobilized between positively charged PAH layers to develop an antibacterial coating that would be cytocompatible with human cells due to NP immobilization. After the application of NPs, the surface was washed off with water before the application of the following PAH layers to ensure the removal of the nonattached NPs. The surfaces treated with PAH/ALG multilayers with CuO and ZnO NPs demonstrated that the NPs were not washed off after the antibacterial experiments and they remained on the stainless-steel surface (Figure S5). On various surfaces, multilayers have been used for NP immobilization for different applications.[35,36,74,83,84] Using various NP immobilization techniques will enhance the safety profile of antibacterial surfaces. NP toxicity is much stronger than the toxicity of dissolved ions,[25] and control of exposure, size,[85] and appropriate surface modifications are crucial factors for minimizing NP toxic while maximizing antibacterial effects.[65] Previously, textiles coated with CuO NPs and PAH/ZnO multilayers demonstrated excellent antibacterial activity against *Staphylococcus aureus*[27] and *Staphylococcus epidermidis*[26] so our further research will be focused on the antibacterial activity of PAH/ALG multilayers with ZnO and CuO NPs against Styphyloccoci.

4. CONCLUSION

Using a holistic approach, the study investigated the antibacterial efficacy and biocompatibility of PAH/ALG polyelectrolyte layers with CuO and ZnO nanoparticles (NPs). The multilayer coatings, particularly those terminating with ALG, influenced bacterial adhesion through surface charge and hydrophobicity changes. Antibacterial tests revealed remarkable differences between CuO and ZnO NPs in their effectiveness against *E. coli*. ZnO NPs, especially rod-like structures, demonstrated superior antibacterial activity. The substantial reduction in *E. coli* viability, > 99%, shows excellent potential for PAH/ALG multilayers with ZnO NPs for antibacterial application.

Conversely, CuO NPs showed limited antibacterial impact, implying their suitability primarily for surface bacteria growth prevention rather than complete eradication. Biocompatibility assessments on human keratinocytes (HaCaT cells) highlighted the safe use of coated surfaces, indicating no significant cytotoxicity even with the release of Cu^{2+} and Zn^{2+} ions. Using polyelectrolyte layers for NP immobilization showcased an effective strategy to minimize NP toxicity while maintaining antibacterial efficacy.

Overall, the research underscores the potential of PAH/ALG polyelectrolyte multilayers with CuO and ZnO NPs, as promising candidates for antibacterial coatings on surfaces. These findings hold significant implications for diverse applications, including medical devices like catheters, where protection against *E. coli* infections is crucial. The study contributes to advancing our understanding of NP-based surface modifications and highlights the potential for practical applications in combating bacterial infections from various surfaces.

■ ASSOCIATED CONTENT

Data Availability Statement

The data that support the findings of this study are available from the corresponding authors upon reasonable request.

Supporting Information

The Supporting Information is available free of charge at https://pubs.acs.org/doi/10.1021/acsanm.4c00981.

Stainless-steel surfaces coated with PAH/ALG multilayers and CuO and ZnO NPs characterized with EDS mapping, Fourier-transformed infrared spectroscopy and scanning electron microscopy (PDF)

■ AUTHOR INFORMATION

Corresponding Authors

Nives Matijaković Mlinarić − *Faculty of Health Sciences, University of Ljubljana, 1000 Ljubljana, Slovenia*; Email: nives.matijakovic@zf.uni-lj.si

Klemen Bohinc − *Faculty of Health Sciences, University of Ljubljana, 1000 Ljubljana, Slovenia*; orcid.org/0000-0003-2126-8762; Email: klemen.bohinc@zf.uni-lj.si

Authors

Stefanie Altenried − *Laboratory for Biointerfaces, Empa, Swiss Federal Laboratories for Materials Science and Technology, 9014 St Gallen, Switzerland*

Atiđa Selmani − *Pharmaceutical Technology and Biopharmacy, Institute of Pharmaceutical Sciences, University of Graz, 8010 Graz, Austria*

Juraj Nikolić − *University of Zagreb Faculty of Science, Department of Chemistry, 10000 Zagreb, Croatia*

Aleksander Učakar − *Jožef Stefan Institute, 1000 Ljubljana, Slovenia*

Anamarija Zore − *Faculty of Health Sciences, University of Ljubljana, 1000 Ljubljana, Slovenia*

Anže Abram − *Jožef Stefan Institute, 1000 Ljubljana, Slovenia*

Sandro Lehner − *Laboratory for Biointerfaces, Empa, Swiss Federal Laboratories for Materials Science and Technology, 9014 St Gallen, Switzerland*

Andrijana Sever Škapin − *Slovenian National Building and Civil Engineering Institute, 1000 Ljubljana, Slovenia*

Monika Kušter − *Jožef Stefan Institute, 1000 Ljubljana, Slovenia*

Eva Roblegg − *Pharmaceutical Technology and Biopharmacy, Institute of Pharmaceutical Sciences, University of Graz, 8010 Graz, Austria*; orcid.org/0000-0002-5553-5147

https://doi.org/10.1021/acsanm.4c00981
ACS Appl. Nano Mater. XXXX, XXX, XXX−XXX

Davor Kovačević − *University of Zagreb Faculty of Science, Department of Chemistry, 10000 Zagreb, Croatia*
Qun Ren − *Laboratory for Biointerfaces, Empa, Swiss Federal Laboratories for Materials Science and Technology, 9014 St Gallen, Switzerland;* orcid.org/0000-0003-0627-761X

Complete contact information is available at: https://pubs.acs.org/10.1021/acsanm.4c00981

Author Contributions

N.M.M.: Funding acquisition, Project administration, Conceptualization, Methodology, Investigation, Formal analysis, Visualization, Writing−original draft, Writing−review and editing; A.S.: Formal analysis, Visualization; S.A.: Formal analysis; J.N.: Formal analysis; A.U.: Formal analysis; A.Z.: Formal analysis; S.L.: Formal analysis; A.S.Š.: Formal analysis; M.K.: Formal analysis; J.V.: Formal analysis; Q.R.: Discussion, Writing−review and editing; E.R.: Discussion, Writing−review and editing; D.K.: Discussion, Writing−review and editing; K.B.: Writing−review and editing. The manuscript was written through contributions of all authors. All authors have given approval to the final version of the manuscript.

Funding

This research was funded by the Slovenian Research and Innovation Agency (ARIS) through the project "Antibacterial and antiviral properties of nanocoated surfaces" N1-0264.

Notes

The authors declare no competing financial interest.

■ ACKNOWLEDGMENTS

N.M.M. would like to thank Dr Maja Mitrović for the help and advice with statistical data analysis. K.B. thanks ARRS through the program Mechanisms of health Maintenance. J.N. would like to thank Vinko Nemec for the help with ATR measurements. A.S.Š. thanks ARRS P2-0273.

■ REFERENCES

(1) Kolář, M. Bacterial Infections, Antimicrobial Resistance and Antibiotic Therapy. *Life* **2022**, *12* (4), 468.
(2) Kaper, J. B.; Nataro, J. P.; Mobley, H. L. T. Pathogenic Escherichia Coli. *Nat. Rev. Microbiol* **2004**, *2* (2), 123−140.
(3) Tuson, H. H.; Weibel, D. B. Bacteria-Surface Interactions. *Soft Matter* **2013**, *9* (17), 4368.
(4) Bezek, K.; Nipič, D.; Torkar, K. G.; Oder, M.; Dražić, G.; Abram, A.; Žibert, J.; Raspor, P.; Bohinc, K. Biofouling of Stainless Steel Surfaces by Four Common Pathogens: The Effects of Glucose Concentration, Temperature and Surface Roughness. *Biofouling* **2019**, *35* (3), 273−283.
(5) Vickery, K.; Hu, H.; Jacombs, A. S.; Bradshaw, D. A.; Deva, A. K. A Review of Bacterial Biofilms and Their Role in Device-Associated Infection. *Healthc Infect* **2013**, *18* (2), 61−66.
(6) Khatoon, Z.; McTiernan, C. D.; Suuronen, E. J.; Mah, T.-F.; Alarcon, E. I. Bacterial Biofilm Formation on Implantable Devices and Approaches to Its Treatment and Prevention. *Heliyon* **2018**, *4* (12), No. e01067.
(7) Percival, S. L.; Suleman, L.; Vuotto, C.; Donelli, G. Healthcare-Associated Infections, Medical Devices and Biofilms: Risk, Tolerance and Control. *J. Med. Microbiol* **2015**, *64* (4), 323−334.
(8) Yılmaz, G. E.; Göktürk, I.; Ovezova, M.; Yılmaz, F.; Kılıç, S.; Denizli, A. Antimicrobial Nanomaterials: A Review. *Hygiene* **2023**, *3* (3), 269−290.
(9) Singh, R.; Lillard, J. W. Nanoparticle-Based Targeted Drug Delivery. *Exp Mol. Pathol* **2009**, *86* (3), 215−223.
(10) Weir, A.; Westerhoff, P.; Fabricius, L.; Hristovski, K.; von Goetz, N. Titanium Dioxide Nanoparticles in Food and Personal Care Products. *Environ. Sci. Technol.* **2012**, *46* (4), 2242−2250.
(11) Stankic, S.; Suman, S.; Haque, F.; Vidic, J. Pure and Multi Metal Oxide Nanoparticles: Synthesis, Antibacterial and Cytotoxic Properties. *J. Nanobiotechnology* **2016**, *14* (73), 1−21.
(12) Slavin, Y. N.; Asnis, J.; Häfeli, U. O.; Bach, H. Metal Nanoparticles: Understanding the Mechanisms behind Antibacterial Activity. *J. Nanobiotechnology* **2017**, *15* (1), 1−21.
(13) Cui, L.; Chen, P.; Chen, S.; Yuan, Z.; Yu, C.; Ren, B.; Zhang, K. In Situ Study of the Antibacterial Activity and Mechanism of Action of Silver Nanoparticles by Surface-Enhanced Raman Spectroscopy. *Anal. Chem.* **2013**, *85* (11), 5436−5443.
(14) Martinez-Gutierrez, F.; Olive, P. L.; Banuelos, A.; Orrantia, E.; Nino, N.; Sanchez, E. M.; Ruiz, F.; Bach, H.; Av-Gay, Y. Synthesis, Characterization, and Evaluation of Antimicrobial and Cytotoxic Effect of Silver and Titanium Nanoparticles. *Nanomedicine* **2010**, *6* (5), 681−688.
(15) Shim, K.; Abdellatif, M.; Choi, E.; Kim, D. Nanostructured ZnO Films on Stainless Steel Are Highly Safe and Effective for Antimicrobial Applications. *Appl. Microbiol. Biotechnol.* **2017**, *101* (7), 2801−2809.
(16) Karbowniczek, J.; Cordero-Arias, L.; Virtanen, S.; Misra, S. K.; Valsami-Jones, E.; Tuchscherr, L.; Rutkowski, B.; Górecki, K.; Bała, P.; Czyrska-Filemonowicz, A.; Boccaccini, A. R. Electrophoretic Deposition of Organic/Inorganic Composite Coatings Containing ZnO Nanoparticles Exhibiting Antibacterial Properties. *Materials Science and Engineering C* **2017**, *77*, 780−789.
(17) Singh, G.; Joyce, E. M.; Beddow, J.; Mason, T. J. Evaluation of Antibacterial Activity of ZnO Nanoparticles. *Journal of Microbiology, Biotechnology and Food Sciences* **2012**, *2* (1), 106−120.
(18) Khlifi, K.; Atallah, M. S.; Cherif, I.; Karkouch, I.; Barhoumi, N.; Attia-Essaies, S. Synthesis of ZnO Nanoparticles and Study of Their Influence on the Mechanical Properties and Antibacterial Activity of PMMA/ZnO Composite for Orthotic Devices. *Surfaces and Interfaces* **2023**, *41*, 103279.
(19) Shekh, M. I.; Patel, K. P.; Patel, R. M. Electrospun ZnO Nanoparticles Doped Core-Sheath Nanofibers: Characterization and Antimicrobial Properties. *J. Polym. Environ* **2018**, *26* (12), 4376−4387.
(20) Maheswari, R. U.; Rani, B. J.; Ravi, G.; Yuvakkumar, R.; Ameen, F.; Al-Sabri, A. Structural, Morphological, Optical and Antibacterial Properties of Pentagon CuO Nanoplatelets. *J. Solgel Sci. Technol.* **2018**, *87* (3), 515−527.
(21) Uma, B.; Anantharaju, K. S.; Renuka, L.; Malini, S.; More, S. S.; Vidya, Y. S.; Meena, S. Synthesis of CuO Samples by Co-Precipitation and Green Mediated Combustion Routes: Comparison of Their Structural, Optical Properties, Photocatalytic, Antibacterial, Haemolytic and Cytotoxic Activities. *Ceram. Int.* **2021**, *47* (7), 10355−10369.
(22) Mohamed, A. A.; Abu-Elghait, M.; Ahmed, N. E.; Salem, S. S. Eco-Friendly Mycogenic Synthesis of ZnO and CuO Nanoparticles for In Vitro Antibacterial, Antibiofilm, and Antifungal Applications. *Biol. Trace Elem Res.* **2021**, *199* (7), 2788−2799.
(23) Dadi, R.; Azouani, R.; Traore, M.; Mielcarek, C.; Kanaev, A. Antibacterial Activity of ZnO and CuO Nanoparticles against Gram Positive and Gram Negative Strains. *Materials Science and Engineering: C* **2019**, *104*, 109968.
(24) Xie, J.; Li, H.; Zhang, T.; Song, B.; Wang, X.; Gu, Z. Recent Advances in ZnO Nanomaterial-Mediated Biological Applications and Action Mechanisms. *Nanomaterials* **2023**, *13* (9), 1500.
(25) Naz, S.; Gul, A.; Zia, M. Toxicity of Copper Oxide Nanoparticles: A Review Study. *IET Nanobiotechnol* **2020**, *14* (1), 1−13.
(26) Najmi, Z.; Matijaković Mlinarić, N.; Calogero Scalia, A.; Cochis, A.; Selmani, A.; Učakar, A.; Abram, A.; Zore, A.; Delač, I.; Jerman, I.; Van de Velde, N.; Vidmar, J.; Bohinc, K.; Rimondini, L. Antibacterial Evaluation of Different Prosthetic Liner Textiles Coated by CuO Nanoparticles. *Heliyon* **2024**, *10* (1), No. e23849.

(27) Matijaković Mlinarić, N.; Wawrzaszek, B.; Kowalska, K.; Selmani, A.; Učakar, A.; Vidmar, J.; Kušter, M.; Van de Velde, N.; Trebše, P.; Sever Škapin, A.; Jerman, I.; Abram, A.; Zore, A.; Roblegg, E.; Bohinc, K. Poly(Allylamine Hydrochloride) and ZnO Nanohybrid Coating for the Development of Hydrophobic, Antibacterial, and Biocompatible Textiles. *Nanomaterials* **2024**, *14* (7), 570.
(28) Erkoc, P.; Uvak, I.; Nazeer, M. A.; Batool, S. R.; Odeh, Y. N.; Akdogan, O.; Kizilel, S. 3D Printing of Cytocompatible Gelatin-Cellulose-Alginate Blend Hydrogels. *Macromol. Biosci* **2020**, *20* (10), 2000106.
(29) Cao, W.; Gao, C. A Hydrogel Adhesive Fabricated from Poly(Ethylene Glycol) Diacrylate and Poly(Allylamine Hydrochloride) with Fast and Spontaneous Degradability and Anti-Bacterial Property. *Polymer (Guildf)* **2020**, *186*, 122082.
(30) Zabielska, J.; Kunicka-Styczyńska, A.; Otlewska, A. Adhesive and Hydrophobic Properties of Pseudomonas Aeruginosa and Pseudomonas Cedrina Associated with Cosmetics. *Ecological Questions* **2018**, *28*, 41.
(31) Kovačević, D.; Pratnekar, R.; Torkar, K. G.; Salopek, J.; Dražić, G.; Abram, A.; Bohinc, K. Influence of Polyelectrolyte Multilayer Properties on Bacterial Adhesion Capacity. *Polymers (Basel)* **2016**, *8* (10), 345−357.
(32) Wang, Y.; You, W.; Song, Y.; Li, X.; Qiu, D.; Cheng, M.; Shi, F. Using a Biocompatible Diazidecrosslinker to Fabricate a Robust Polyelectrolyte Multilayer Film with Enhanced Effects on Cell Proliferation. *J. Mater. Chem. B* **2017**, *5* (2), 375−381.
(33) Ahmad Raus, R.; Wan Nawawi, W. M. F.; Nasaruddin, R. R. Alginate and Alginate Composites for Biomedical Applications. *Asian J. Pharm. Sci.* **2021**, *16* (3), 280−306.
(34) Elahi, M.; Guan, G.; Wang, L.; King, M. Influence of Layer-by-Layer Polyelectrolyte Deposition and EDC/NHS Activated Heparin Immobilization onto Silk Fibroin Fabric. *Materials* **2014**, *7* (4), 2956−2977.
(35) Yuan, W.; Fu, J.; Su, K.; Ji, J. Self-Assembled Chitosan/Heparin Multilayer Film as a Novel Template for in Situ Synthesis of Silver Nanoparticles. *Colloids Surf. B Biointerfaces* **2010**, *76* (2), 549−555.
(36) Yuan, W.; Lu, Z.; Li, C. M. Self-Assembling Microsized Materials to Fabricate Multifunctional Hierarchical Nanostructures on Macroscale Substrates. *J. Mater. Chem. A Mater.* **2013**, *1* (21), 6416.
(37) Tidim, G.; Guzel, M.; Soyer, Y.; Erel-Goktepe, I. Layer-by-Layer Assembly of Chitosan/Alginate Thin Films Containing Salmonella Enterica Bacteriophages for Antibacterial Applications. *Carbohydr. Polym.* **2024**, *328*, 121710.
(38) AL-Ali, N.; Abdulkareem, M.; Anoon, I. Antibacterial Improvement with Multilayer of Bio-Composite Coatings Produced by Electrophoretic Deposition. *Engineering and Technology Journal* **2024**, *0* (0), 1−12.
(39) Rodriguez Maya, S.; Restrepo Posada, M.; Lenis Rodas, J. A.; Bejarano Gaitan, G.; Bolívar Osorio, F. J. Microstructural and Tribological Properties of TiO2/Ag Multilayer Coatings Using Magnetron Sputtering Technique for Potential Applications in Non-Permanent Implants. *Thin Solid Films* **2024**, *789*, 140168.
(40) Karami, R.; Moradipour, P.; Arkan, E.; Zarghami, R.; Rashidi, K.; Darvishi, E. Biocompatible Nano-Bandage Modified with Silver Nanoparticles Based on Herbal for Burn Treatment. *Polym. Bull.* **2023**, DOI: 10.1007/s00289-023-05093-w.
(41) Xiao, Z.; Liu, L. H.; Liu, T.; Yang, D.; Jia, X.; Du, Y. K.; Li, S. Q.; Yang, W. J.; Xi, Y. M.; Zeng, R. C. Degradation and Biocompatibility of Genipin Crosslinked Polyelectrolyte Films on Biomedical Magnesium Alloy via Layer-by-Layer Assembly. *Prog. Org. Coat.* **2023**, *175*, 107372.
(42) Shamhari, N. M.; Wee, B. S.; Chin, S. F.; Kok, K. Y. Synthesis and Characterization of Zinc Oxide Nanoparticles with Small Particle Size Distribution. *Acta Chim Slov* **2018**, *65* (3), 578−585.
(43) Abram, A.; Zore, A.; Lipovž, U.; Košak, A.; Gavras, M.; Boltežar, Ž.; Bohinc, K. Bacterial Adhesion on Prosthetic and Orthotic Material Surfaces. *Coatings* **2021**, *11* (12), 1469.
(44) Arun, K. J.; Batra, A. K.; Krishna, A.; Bhat, K.; Aggarwal, M. D.; Joseph Francis, P. J. Surfactant Free Hydrothermal Synthesis of Copper Oxide Nanoparticles. *American Journal of Materials Science* **2015**, *5* (3A), 36−38.
(45) Ramimoghadam, D.; Bin Hussein, M. Z.; Taufiq-Yap, Y. H. Hydrothermal Synthesis of Zinc Oxide Nanoparticles Using Rice as Soft Biotemplate. *Chem. Cent J.* **2013**, *7* (1), 136.
(46) Bueno-Ferrer, C.; Parres-Esclapez, S.; Lozano-Castelló, D.; Bueno-López, A. Relationship between Surface Area and Crystal Size of Pure and Doped Cerium Oxides. *Journal of Rare Earths* **2010**, *28* (5), 647−653.
(47) Zou, Y.; Li, Y.; Zhang, N.; Liu, X. Flower-like CuO Synthesized by CTAB-Assisted Hydrothermal Method. *Bulletin of Materials Science* **2011**, *34* (4), 967−971.
(48) Naz, S.; Tabassum, S.; Freitas Fernandes, N.; Mujahid, M.; Zia, M.; Carcache de Blanco, E. J. Anticancer and Antibacterial Potential of Rhus Punjabensis and CuO Nanoparticles. *Nat. Prod Res.* **2020**, *34* (5), 720−725.
(49) Chico, B.; Martinez, L.; Pérez, F. J. Nitrogen Ion Implantation on Stainless Steel: AFM Study of Surface Modification. *Appl. Surf. Sci.* **2005**, *243* (1−4), 409−414.
(50) Nikolić, J.; Ivančić, A.; Klačić, T.; Kovačević, D. Synthetic versus Natural Precursor Layer: A Study on the Properties of Biocompatible Chitosan/Carboxymethyl Cellulose Nanofilms. *ACS Omega* **2023**, *8* (22), 20031−20041.
(51) Bohinc, K.; Dražić, G.; Abram, A.; Jevšnik, M.; Jeršek, B.; Nipič, D.; Kurinčič, M.; Raspor, P. Metal Surface Characteristics Dictate Bacterial Adhesion Capacity. *Int. J. Adhes Adhes* **2016**, *68*, 39−46.
(52) Daemi, H.; Barikani, M. Synthesis and Characterization of Calcium Alginate Nanoparticles, Sodium Homopolymannuronate Salt and Its Calcium Nanoparticles. *Scientia Iranica* **2012**, *19* (6), 2023−2028.
(53) Molino Cornejo, J. J.; Matsuoka, E.; Daiguji, H. Size Control of Hollow Poly-Allylamine Hydrochloride/Poly-Sodium Styrene Sulfonate Microcapsules Using the Bubble Template Method. *Soft Matter* **2011**, *7* (5), 1897.
(54) Katsikogianni, M.; Missirlis, Y. Concise Review of Mechanisms of Bacterial Adhesion to Biomaterials and of Techniques Used in Estimating Bacteria-Material Interactions. *Eur. Cell Mater.* **2004**, *8*, 37−57.
(55) Kozmos, M.; Virant, P.; Rojko, F.; Abram, A.; Rudolf, R.; Raspor, P.; Zore, A.; Bohinc, K. Bacterial Adhesion of Streptococcus Mutans to Dental Material Surfaces. *Molecules* **2021**, *26* (4), 1152.
(56) Ribeiro, M.; Monteiro, F. J.; Ferraz, M. P. Infection of Orthopedic Implants with Emphasis on Bacterial Adhesion Process and Techniques Used in Studying Bacterial-Material Interactions. *Biomatter* **2012**, *2* (4), 176−194.
(57) Preedy, E.; Perni, S.; Nipic, D.; Bohinc, K.; Prokopovich, P. Surface Roughness Mediated Adhesion Forces between Borosilicate Glass and Gram-Positive Bacteria. *Langmuir* **2014**, *30* (31), 9466−9476.
(58) Hamadi, F.; Latrache, H.; Zahir, H.; Elghmari, A.; Timinouni, M.; Ellouali, M. The Relation between Escherichia Coli Surface Functional Groups' Composition and Their Physicochemical Properties. *Brazilian Journal of Microbiology* **2008**, *39* (1), 10−15.
(59) Kozmos, M.; Virant, P.; Rojko, F.; Abram, A.; Rudolf, R.; Raspor, P.; Zore, A.; Bohinc, K. Bacterial Adhesion of Streptococcus Mutans to Dental Material Surfaces. *Molecules* **2021**, *26* (4), 1152.
(60) Barbera, L.; De Plano, L. M.; Franco, D.; Gattuso, G.; Guglielmino, S. P. P.; Lando, G.; Notti, A.; Parisi, M. F.; Pisagatti, I. Antiadhesive and Antibacterial Properties of Pillar[5]Arene-Based Multilayers. *Chem. Commun.* **2018**, *54* (72), 10203−10206.
(61) O'Connor, N. A.; Abugharbieh, A.; Yasmeen, F.; Buabeng, E.; Mathew, S.; Samaroo, D.; Cheng, H. P. The Crosslinking of Polysaccharides with Polyamines and Dextran-Polyallylamine Antibacterial Hydrogels. *Int. J. Biol. Macromol.* **2015**, *72*, 88−93.
(62) Semisch, A.; Ohle, J.; Witt, B.; Hartwig, A. Cytotoxicity and Genotoxicity of Nano - and Microparticulate Copper Oxide: Role of Solubility and Intracellular Bioavailability. *Part Fibre Toxicol* **2014**, *11* (1), 10.

https://doi.org/10.1021/acsanm.4c00981
ACS Appl. Nano Mater. XXXX, XXX, XXX−XXX

(63) Pasquet, J.; Chevalier, Y.; Pelletier, J.; Couval, E.; Bouvier, D.; Bolzinger, M. A. The Contribution of Zinc Ions to the Antimicrobial Activity of Zinc Oxide. *Colloids Surf. A Physicochem Eng. Asp* **2014**, *457* (1), 263−274.
(64) Ginjupalli, K.; Alla, R.; Shaw, T.; Tellapragada, C.; Kumar Gupta, L.; Upadhya, N. *Comparative Evaluation of Efficacy of Zinc Oxide and Copper Oxide Nanoparticles as Antimicrobial Additives in Alginate Impression Materials*; 2018; Vol. *5*. www.sciencedirect.comwww.materialstoday.com/proceedings.
(65) Chang, Y.-N.; Zhang, M.; Xia, L.; Zhang, J.; Xing, G. The Toxic Effects and Mechanisms of CuO and ZnO Nanoparticles. *Materials* **2012**, *5* (12), 2850−2871.
(66) Godoy-Gallardo, M.; Eckhard, U.; Delgado, L. M.; de Roo Puente, Y. J. D.; Hoyos-Nogués, M.; Gil, F. J.; Perez, R. A. Antibacterial Approaches in Tissue Engineering Using Metal Ions and Nanoparticles: From Mechanisms to Applications. *Bioact Mater.* **2021**, *6* (12), 4470−4490.
(67) Wu, Y.; Wu, W.; Zhao, W.; Lan, X. Revealing the Antibacterial Mechanism of Copper Surfaces with Controllable Microstructures. *Surf. Coat. Technol.* **2020**, *395*, 125911.
(68) Emam, H. E.; Ahmed, H. B.; Bechtold, T. In-Situ Deposition of Cu2O Micro-Needles for Biologically Active Textiles and Their Release Properties. *Carbohydr. Polym.* **2017**, *165*, 255−265.
(69) Vincent, M.; Duval, R. E.; Hartemann, P.; Engels-Deutsch, M. Contact Killing and Antimicrobial Properties of Copper. *J. Appl. Microbiol.* **2018**, *124*, 1032−1046.
(70) Kadiyala, U.; Turali-Emre, E. S.; Bahng, J. H.; Kotov, N. A.; VanEpps, J. S. Unexpected Insights into Antibacterial Activity of Zinc Oxide Nanoparticles against Methicillin Resistant: Staphylococcus Aureus (MRSA). *Nanoscale* **2018**, *10* (10), 4927−4939.
(71) Raghupathi, K. R.; Koodali, R. T.; Manna, A. C. Size-Dependent Bacterial Growth Inhibition and Mechanism of Antibacterial Activity of Zinc Oxide Nanoparticles. *Langmuir* **2011**, *27* (7), 4020−4028.
(72) Joe, A.; Park, S. H.; Shim, K. D.; Kim, D. J.; Jhee, K. H.; Lee, H. W.; Heo, C. H.; Kim, H. M.; Jang, E. S. Antibacterial Mechanism of ZnO Nanoparticles under Dark Conditions. *Journal of Industrial and Engineering Chemistry* **2017**, *45*, 430−439.
(73) Kong, H. Designing Alginate Hydrogels to Maintain Viability of Immobilized Cells. *Biomaterials* **2003**, *24* (22), 4023−4029.
(74) Wang, P.; Kankala, R. K.; Chen, B.; Long, R.; Cai, D.; Liu, Y.; Wang, S. Poly-allylamine Hydrochloride and Fucoidan-based Self-assembled Polyelectrolyte Complex Nanoparticles for Cancer Therapeutics. *J. Biomed Mater. Res. A* **2019**, *107* (2), 339−347.
(75) Alekseenko, L.; Shilina, M.; Kozhukharova, I.; Lyublinskaya, O.; Fridlyanskaya, I.; Nikolsky, N.; Grinchuk, T. Impact of Polyallylamine Hydrochloride on Gene Expression and Karyotypic Stability of Multidrug Resistant Transformed Cells. *Cells* **2020**, *9* (10), 2332.
(76) Janeesh, P. A.; Sami, H.; Dhanya, C. R.; Sivakumar, S.; Abraham, A. Biocompatibility and Genotoxicity Studies of Polyallylamine Hydrochloride Nanocapsules in Rats. *RSC Adv.* **2014**, *4* (47), 24484−24497.
(77) Poortinga, A. T.; Bos, R.; Norde, W.; Busscher, H. J. Electric Double Layer Interactions in Bacterial Adhesion to Surfaces. *Surf. Sci. Rep* **2002**, *47* (1), 1−32.
(78) Bolster, C. H.; Haznedaroglu, B. Z.; Walker, S. L. Diversity in Cell Properties and Transport Behavior among 12 Different Environmental *Escherichia Coli* Isolates. *J. Environ. Qual* **2009**, *38* (2), 465−472.
(79) Liang, X.; Liao, C.; Thompson, M. L.; Soupir, M. L.; Jarboe, L. R.; Dixon, P. M. E. Coli Surface Properties Differ between Stream Water and Sediment Environments. *Front Microbiol* **2016**, *7*, 1732.
(80) Morrow, J. B.; Stratton, R.; Yang, H.-H.; Smets, B. F.; Grasso, D. Macro- and Nanoscale Observations of Adhesive Behavior for Several *E. Coli* Strains (O157:H7 and Environmental Isolates) on Mineral Surfaces. *Environ. Sci. Technol.* **2005**, *39* (17), 6395−6404.
(81) Adair, J. H.; Suvaci, E.; Sindel, J. Surface and Colloid Chemistry. In *Encyclopedia of Materials: Science and Technology*; Elsevier, 2001; pp 1−10. DOI: 10.1016/B0-08-043152-6/01622-3.
(82) Rijnaarts, H. H. M.; Norde, W.; Bouwer, E. J.; Lyklema, J.; Zehnder, A. J. B. Bacterial Deposition in Porous Media: Effects of Cell-Coating, Substratum Hydrophobicity, and Electrolyte Concentration. *Environ. Sci. Technol.* **1996**, *30* (10), 2877−2883.
(83) Marković, D.; Petkovska, J.; Mladenovic, N.; Radoičić, M.; Rodriguez-Melendez, D.; Ilic-Tomic, T.; Radetić, M.; Grunlan, J. C.; Jordanov, I. Antimicrobial and < scp > UV</scp> Protective Chitosan/Lignin Multilayer Nanocoating with Immobilized Silver Nanoparticles. *J. Appl. Polym. Sci.* **2023**, *140* (19), e53823.
(84) Xiao, S.; Wu, S.; Shen, M.; Guo, R.; Huang, Q.; Wang, S.; Shi, X. Polyelectrolyte Multilayer-Assisted Immobilization of Zero-Valent Iron Nanoparticles onto Polymer Nanofibers for Potential Environmental Applications. *ACS Appl. Mater. Interfaces* **2009**, *1* (12), 2848−2855.
(85) Motelica, L.; Vasile, B. S.; Ficai, A.; Surdu, A. V.; Ficai, D.; Oprea, O. C.; Andronescu, E.; Jinga, D. C.; Holban, A. M. Influence of the Alcohols on the ZnO Synthesis and Its Properties: The Photocatalytic and Antimicrobial Activities. *Pharmaceutics* **2022**, *14* (12), 2842.

https://doi.org/10.1021/acsanm.4c00981
ACS Appl. Nano Mater. XXXX, XXX, XXX−XXX